Series-Fed Beam-Steerable Millimeter-Wave Antenna Design With Wide Spatial Coverage for 5G Mobile Terminals

Changjiang Deng, *Member, IEEE*, Di Liu, Behzad Yektakhah, *Student Member, IEEE*, and Kamal Sarabandi, *Fellow, IEEE*

***Abstract*— A low-cost beam-steerable antenna operating at 28 GHz is presented for 5G mobile terminal applications. The proposed array has a sandwich-like stack structure, including ten patch elements, a ground plane with two rows of slots, and a long microstrip transmission feed line. The radiators and the transmission line are placed at the two sides of the ground plane, which provides great flexibility in designing the radiating pattern and the feed network. Switches are added on the transmission line to construct periodic distributed phase shifters for beam steering. The 2 bit phase shifter with phases of 0°, 90°, 180°, and 270° is formed without using phase delay lines. Continuous beam steering is achieved, and the steerable angle is 121° in the upper hemisphere. Two location configurations of the proposed array in 5G mobile terminals are analyzed and the angular coverage range is evaluated. The array can cover 38.8% of the hemispherical space with a gain threshold of 10 dBi.**

***Index Terms*— 5G communication, beam steering, millimeter-wave (mm-wave) antennas, mobile terminal antennas.**

I. Introduction

MILLIMETER-WAVE (mm-wave) band will play an important role in the upcoming 5G mobile communication, since it offers unprecedented bandwidth and gigabit-per-second (Gb/s) data rates [1]–[3]. The 28 GHz frequency band is a prime candidate for 5G mm-wave communication, which has been allocated as the experimental band in many countries [4]. The typical scenario of 5G mm-wave communication is shown in Fig. 1. On one hand, the antenna in the base station generates beams in all directions to cover the direction of the mobile terminals. On the other hand, the beam direction of the mobile terminal antenna should be steerable because of the antenna's random orientation. High gain is required for both base stations and mobile terminals to overcome the large free-space path loss at mm-wave frequencies. In addition, the antenna of 5G mobile terminal has more restrictions. Wide spatial coverage is preferred to establish stable link connection in complex environment; low power consumption and low cost are necessary considering the portability and massive production of the device [5]. Therefore, it is challenging to design high gain, wide spatial coverage, and low-cost mm-wave antenna for 5G mobile terminals.

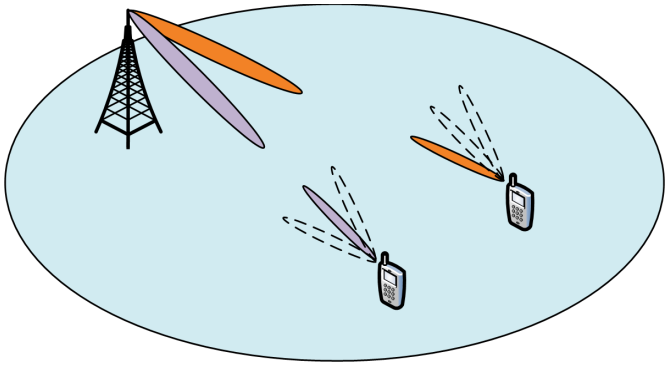

Fig. 1. Typical scenario of 5G mm-wave communication.

Phased array beam-steering approach is the key technique to steer the beam. By controlling the feed amplitude and phase of each element, the beam direction of the array can be precisely set. Based on this principle, one straightforward method is connecting each antenna element with a transceiver. However, this approach is complex and costly to implement. For 5G mobile terminal applications, the focus is on the integration of multiple channels within a single chip. Recently, significant progress has been made, and development of few mm-wave chips operating at 28 GHz band has been launched [6]–[8]. Apart from the transceiver, the array in mobile terminal also needs careful consideration, due to the requirement of wide spatial coverage. Various phased arrays with different kinds of radiators have been proposed [9]–[18]. For example, a high-gain phased patch array is designed in [17]. The angular range of steerable beam of the array is about 90°. For this design, four arrays are needed to achieve full azimuthal coverage. Elements with wide beamwidth are then designed to extend the spatial coverage of array. Dipole, monopole, and slot arrays

Manuscript received May 24, 2019; revised October 29, 2019; accepted December 13, 2019. Date of publication January 8, 2020; date of current version May 5, 2020. This work was supported in part by the National Natural Science Foundation of China under Contract 61701024, and in part by the China Scholarship Council (CSC) and the State Key Laboratory of Millimeter Waves under Contract K201902. *(Corresponding author: Changjiang Deng.)*

Changjiang Deng and Di Liu are with the Beijing Key Laboratory of Millimeter Wave and Terahertz Technology, School of Information and Electronics, Beijing Institute of Technology, Beijing 100081, China (e-mail: dengcj11@bit.edu.cn; 15317300930@163.com).

Behzad Yektakhah and Kamal Sarabandi are with the Radiation Laboratory, Department of Electrical Engineering and Computer Science, University of Michigan, Ann Arbor, MI 48109-2122 USA (e-mail: byekta@umich.edu; saraband@eecs.umich.edu).

Color versions of one or more of the figures in this article are available online at http://ieeexplore.ieee.org.

Digital Object Identifier 10.1109/TAP.2019.2963583

are popular, which can steer the beam over 150°. However, this can be achieved at the cost of etching slot on the chassis ground or requiring certain ground clearance. In this method, the interconnection between the transceiver and the array may also cause mismatch and extra loss, since the two parts are designed separately.

To reduce the cost of the phased array, some alternative solutions have been proposed without using multiple transceivers. Multibeam technique is promising to achieve high cost-effective beam steering [19]–[23]. The desired phase shift of the array is fixed by using passive beam-forming network, thus active phase shifter can be eliminated. For example, a 1×8 dipole array fed by an 8×8 Butler matrix is proposed in [19] to generate eight beams. The beam-forming network is fabricated using planar substrate-integrated waveguide (SIW) technique. However, the beams are fixed and switches are needed to switch among the multiple beams. Array with driven and parasitic elements is another attractive solution to achieve low-cost beam steering [24], [25]. The phase of the array is changed by loading different reactive impedance on the parasitic elements. In [25], a compact array with one driven and two parasitic monopoles is proposed. The main beam of the array has four directions by controlling the loading length of the parasitic elements. Nevertheless, the two methods suffer from limited beam positioning states.

Leaky-wave antenna is a well-known beam-steering antenna without using power divider and phase shifter. The main beam of leaky-wave antenna will steer with the change of frequency, because of the periodic phase distribution on the transmission line [26]. In order to achieve beam steering at fixed frequency, electronic switches are introduced in leaky-wave antennas [27]–[34]. The phase distribution of the transmission line can be disturbed by the switches, which will change the direction of the main beam. For instance, a fixed-frequency beam-steering microstrip leaky-wave antenna is presented in [28]. p-i-n switches are loaded at the edge of the microstrip line. The steerable angle is 29°. In [30], varactor diodes are used to achieve continuous beam steering. The steering range is extended to 45°. In [31], the microstrip line structure is modified and bit phase shifters are constructed. The overall steered angle achieves 94°. However, this series-fed technique is yet to be applied to 5G mm-wave mobile terminal design. In addition, the spatial coverage is still insufficient and the steerable angle needs to be increased.

In this article, an electrically beam-switchable leaky-wave antenna is proposed for 5G mm-wave communication. The radiating array and the feed network are separated by the ground plane, series-fed structure and switches are used to construct low-loss phase shifters. The arrangement of the array in mobile terminal is also discussed. This article is organized as follows. Section II presents the design of the beam-switchable patch array and the operating principle of the array is analyzed. Section III analyzes the impact of practical switches. Section IV presents the experimental results where steering at different beam angles are verified. Section V analyzes the spatial coverage of the array in 5G mobile terminal. Finally, Section VI draws the conclusion of this work.

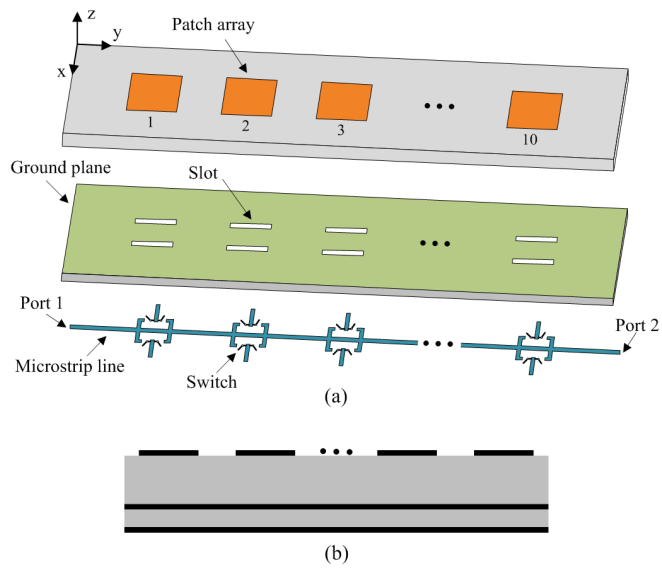

Fig. 2. Geometry of the proposed phased array. (a) 3-D exploded view. (b) Side view.

II. Series-Fed Beam-Steerable Antenna Design

A. Antenna Geometry

The geometry of the proposed phased array is shown in Fig. 2. It includes two tightly stacked substrate layers. The upper substrate layer is made of RT/duroid 5880 ($\varepsilon_r = 2.2$, $\tan\delta = 0.0009$), with a thickness of 0.787 mm. The lower substrate layer is made of RO4003C ($\varepsilon_r = 3.55$, $\tan\delta = 0.002$), with a thickness of 0.203 mm. There are three metal layers printed on the two substrate layers. The radiating patch array is on the top metal layer, which has ten uniformly distributed elements. The ground plane is on the middle metal layer. Two rows of slots are symmetrically etched along the y-axis. The feed network is on the bottom metal layer. It consists of a microstrip transmission line and ten periodic distributed structures. Each structure has four branches that are extended from the two sides of the microstrip line and two floating branches that cross the pair of slots above them. Binary switches are used to control the connection of the branches. The periodic distributed structures are equivalent to a series of 2 bit phase shifters, which will be explained later. In this design, the radiating array and feed network are isolated by the ground plane, and energies are coupled via the slots.

The proposed design can be viewed as a 1-D series-fed array with ten elements. The dimensions of element are shown in Fig. 3. Each element consists of a patch, two parallel slots, and a 2 bit phase shifter. Four switches are used to control the state of the phase shifter. The impedance of the transmission line is 50 Ω. The parameters are optimized with the software HFSS version 15 and are listed in Table I.

B. Reconfigurable Element Design

The radiating structure of the element is an aperture-coupled patch. The radiation pattern of the patch is mainly determined by the feed line beneath the slot. As shown in Fig. 3, the switches control the connection of the floating branches and

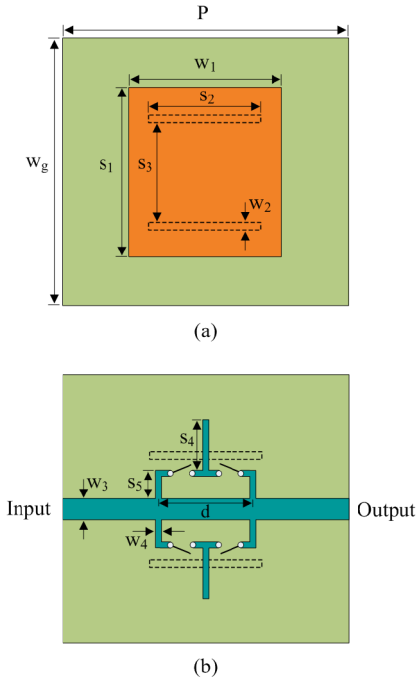

Fig. 3. Geometry and parameters of one element of the array. (a) Top view. (b) Bottom view.

TABLE I
DETAILED DIMENSIONS OF THE ELEMENT SHOWN IN FIG. 3 (UNIT: mm)

P	W_g	s_1	w_1	s_2	w_2
4.8	10	2.6	2.2	2	0.2
s_3	w_3	s_4	w_4	s_5	d
1.2	0.44	1.4	0.2	0.37	1.8

the branches extended from the transmission line. The path is connected, if the corresponding switch is ON. Signals will flow along the path and energies will be coupled to the patch via the slot above the path. To obtain broadside radiation pattern, only one switch is ON during the reconfigurable process.

The energy coupled from the transmission line is determined by the width of the branches. As the linewidth increases, the impedance of the branches decreases, the branches will get more energy from the transmission line, that is, the leak rate is increased. However, the increase of the leak rate will deteriorate the impedance match of the transmission line. Fig. 4 shows the simulated S-parameters of one element of the array when one switch is ON. It is shown that the leak rate is within 1 dB (about 20%), and the input impedance is well matched. It should be mentioned that in this simulation, the ON and OFF states of the switches are assumed ideal to simplify the analysis.

As shown in Fig. 5, the element has broadside radiation patterns, no matter which switch is ON. However, the phase of the radiated field is different. The near field above the patch is observed to depict the phase variation. As shown in Fig. 6(a), the observation point is located at the z-axis and is about $0.2\lambda_0$ (λ_0 is the free-space wavelength at 28 GHz) away from the patch. The four switches in Fig. 6(b) can be

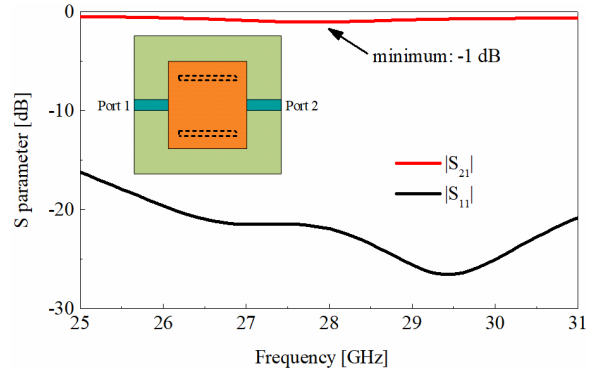

Fig. 4. Simulated S-parameters of a single element when one switch is ON.

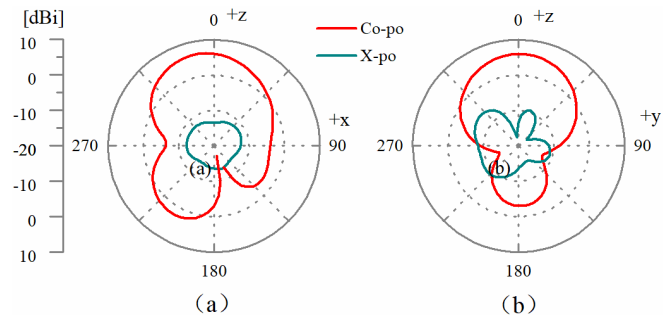

Fig. 5. Radiation patterns of the element at 28 GHz. (a) E-plane. (b) H-plane.

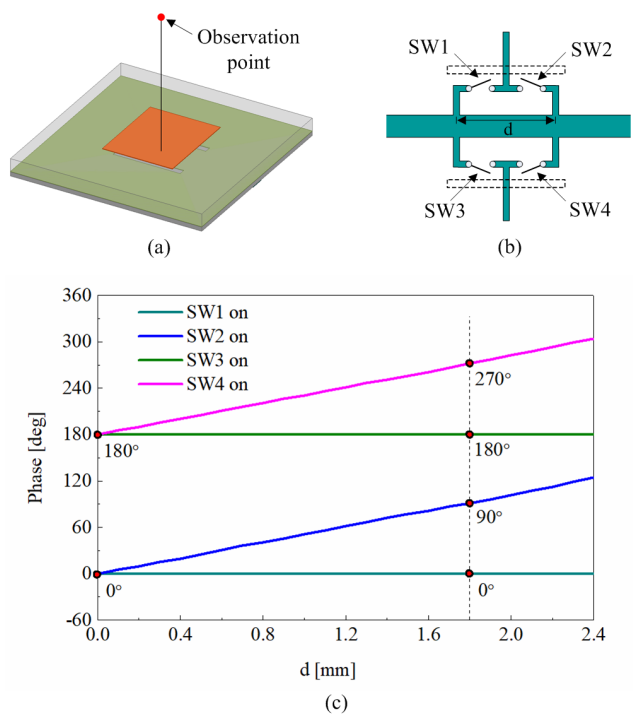

Fig. 6. Near-field observation. (a) Observation point. (b) 2 bit phase shifter. (c) Near-field phase with different offset distances.

divided into two groups. SW1 and SW2 are at one side, and SW3 and SW4 are at the other side of the transmission line. The offset distance between the two switches in each group has a significant influence on the phase. Fig. 6(c) shows the observed phase with different offset distances. The switches

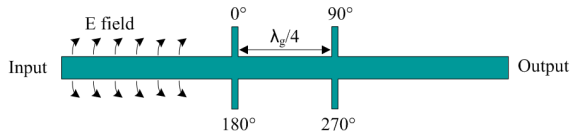

Fig. 7. Four phase states of the 2 bit phase shifter.

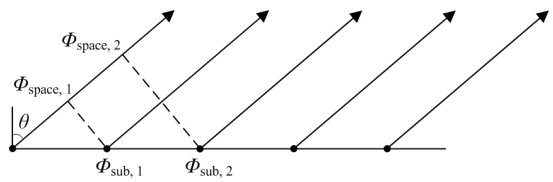

Fig. 8. Phase front of the 1-D phased array.

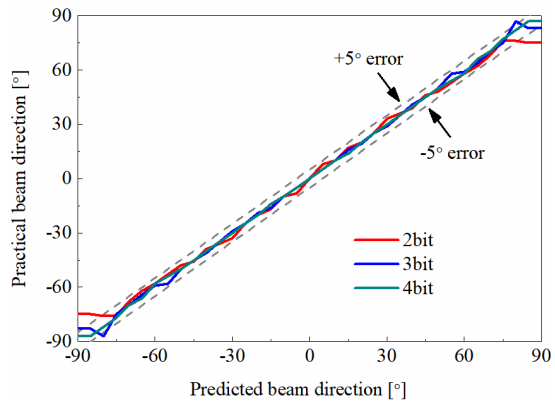

Fig. 9. Influence of phase error on beam direction of ten-element array.

have four states and in each state, one switch is ON and the other three are OFF. Only two switches are required, when the offset distance is zero. It is shown that there is a 180° phase difference between the two states, which implies that the two switches form a 1 bit phase shifter. As the offset distance increases, the phase difference for the switches in the same group become larger, while the phase difference between the two groups remains 180°. Phases of 0°, 90°, 180°, and 270° are desired among the four states, when the distance is 1.8 mm (about $\lambda_g/4$, λ_g is the wavelength in substrate at 28 GHz). It indicates that an equivalent 2 bit phase shifter is constructed in this way.

The operating principle of the 2 bit phase shifter is analyzed. As shown in Fig. 7, the electric fields at the two sides of the microstrip line are 180° out of phase. It leads to a natural 180° phase shift. In addition, the transmission line has a periodic phase distribution. There is a 90° phase delay when the wave travels a distance of $\lambda_g/4$. Therefore, we can introduce four branches at the four positions to generate 0°, 90°, 180°, and 270° without using traditional phase delay lines.

C. Beam Steering of the Array

Based on the proposed reconfigurable array element, the radiation patterns of the phased array are calculated. Fig. 8 shows the wave propagation of the 1-D phased array. According to the phased array theory, the waves on the dashed line should have equal phase delay to make sure that the main beam will point to the specified angle θ. On one hand, the phase delay of element n in free space is expressed as follows:

$$\phi_{space,n} = -n \times k_0 \times P \times \sin(\theta), \quad n = 1 \ldots 10 \tag{1}$$

where k_0 is the wavenumber in free space and P is the periodic spacing between the elements.

On the other hand, the microstrip transmission line supports a periodic phase distribution along the line. The phase delay at element n is

$$\phi_{sub,n} = -n \times k_g \times P \tag{2}$$

where k_g is the wavenumber in the substrate.

In order to satisfy the equal phase condition, the required phase compensation for element n should be

$$\begin{aligned}\phi_{comp,n} &= \phi_{space,n} - \phi_{sub,n} \\ &= n \times P \times (k_g - k_0 \sin(\theta)).\end{aligned} \tag{3}$$

This value can be mapped to the range of 0°–360° because the phase is periodic. Then, the required phase needs to be quantized by using the 2 bit phase shifter as follows:

$$\phi_{qua,n} = \begin{cases} 90°, & \text{if } 45° \le \phi_{comp,n} < 135° \\ 180°, & \text{if } 135° \le \phi_{comp,n} < 225° \\ 270°, & \text{if } 225° \le \phi_{comp,n} < 315° \\ 0, & \text{else.} \end{cases} \tag{4}$$

Obviously, the sampled phase value has a maximal error of 45°. To investigate the quantization error of phase shifter on beam direction, Fig. 9 shows the beam direction of ten-element array with different bit phase shifters. The difference between predicted value and practical value becomes small, as the bit number increases. The maximal beam shift is within 5° in all the three cases. Considering that the accuracy requirement of beam direction is low for mobile terminal, 2 bit phase shifter is adopted to reduce the cost.

In this specific design, the interelement space is about $0.44\lambda_0$. The corresponding electrical length is $3\lambda_g/4$ in substrate. Using (1) and (4) and the array parameters, the steering angle can be calculated and simulated. Fig. 10 shows the steered beam in the plane that contains the array. The calculated steering step is 10°, and the angle ranges from −80° to 80°. It is seen that the simulated beam direction agrees well with the calculated value, when the beam is near the broadside direction. As the beam steers toward the endfire direction, the beam becomes difficult to tilt. The simulated steerable angle range is smaller than the calculated angle range. The reason is that the mutual coupling among elements becomes strong as the beam direction approaches the horizontal plane.

D. Reflection Cancellation for Gain Enhancement

It is well known that leaky-wave antennas suffer from gain drop at the broadside direction, where all the elements are excited in phase. Basically, the powers reflected from elements

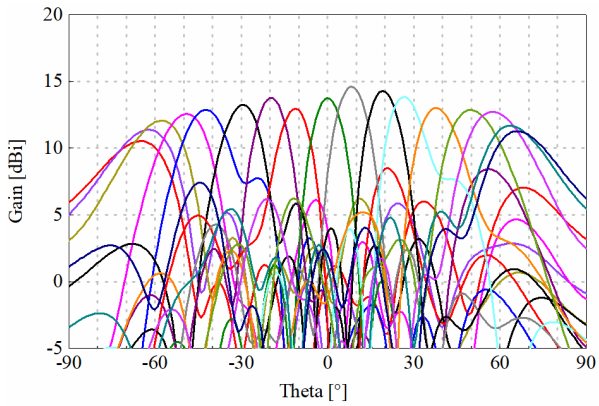

Fig. 10. Simulated beam steering of the ten-element array at 28 GHz.

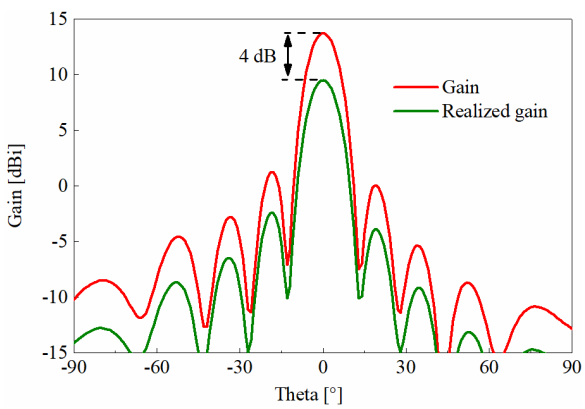

Fig. 11. Gain and the realized gain of the array with broadside beam showing the effect of significant impedance mismatch that occurs when the beam is directed along the broadside direction.

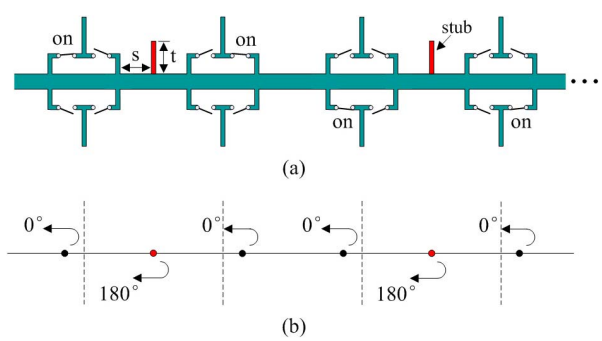

Fig. 12. Broadside gain enhancement. (a) Reflection cancellation stubs and switch configuration for broadside radiation. (b) Diagram showing the mechanism of the reflection cancellation method.

will add together coherently at the input port, leading to strong impedance mismatch. This behavior is also observed in the proposed array. Fig. 11 shows the influence of the input mismatch in realizable gain. The realized gain drops about 4 dB when the impedance match is taken into consideration.

To circumvent this difficulty, compensation structures are introduced to reduce the mismatch of in-phase excitation. Fig. 12(a) shows the modified feed network, where five small stubs are added among the ten phase shifters. These stubs create reflections that are equal and out of phase with reflections

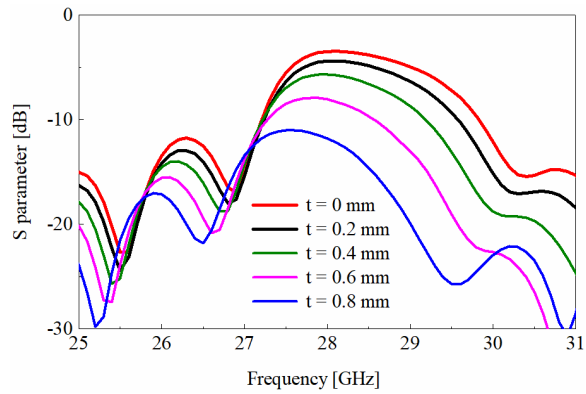

Fig. 13. Effect of the length of the reflection cancellation stubs on S_{11}.

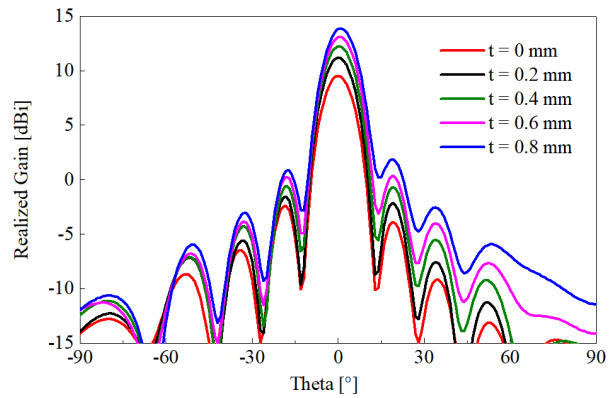

Fig. 14. Effect of the length of the reflection cancellation stubs on realized broadside gain at 28 GHz.

produced by the phase shifters. Fig. 12(b) shows the concept of phase cancellation. For the optimal reflection cancellation, the parameters of the stub are found to be s = 1.8 mm, t = 0.6 mm. The switches are configured to obtain broadside radiation. It is noted that the reflecting positions of elements are not uniformly distributed. The distance between adjacent reflections is either $\lambda_g/2$ or λ_g. There is a stub located at the center of the two reflections if the distance is λ_g. It introduces extra reflection with phase of 180°. Therefore, the reflections from the stubs and the elements are out of phase. The reflection cancelation is helpful to reduce the mismatch.

The reflection level of the reflection cancellation stubs is controlled by changing the length of the stub. Figs. 13 and 14 show the effect of the stub on the input impedance match and the realized gain. It is shown that the impedance match becomes better as the length of the stub increases. The realized broadside gain at 28 GHz also increases with the increase in the length. However, it should be noted that the introduction of the stub will affect the phase distributions on the transmission line. Other beam states are influenced if the reflection from the stub is strong. The stub length value of 0.6 mm is adopted, which considers tradeoff in realizable gain among all the beam states.

The beam steering with reflection cancellation structure at 27, 28, and 29 GHz is shown in Figs. 15–17. The peak gain at 28 GHz is 12.8 dBi at the broadside direction, and the maximal

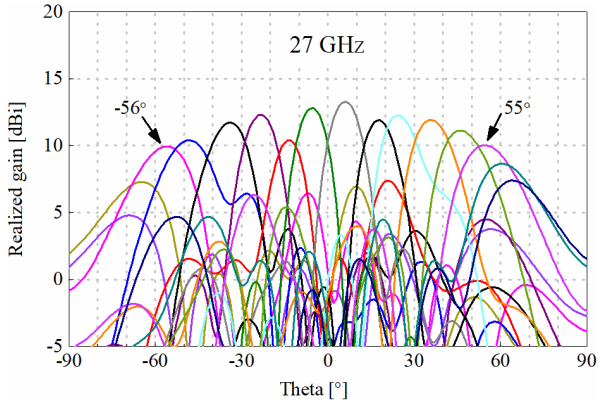

Fig. 15. Simulated beam steering of the ten-element array with reflection cancellation stubs at 27 GHz.

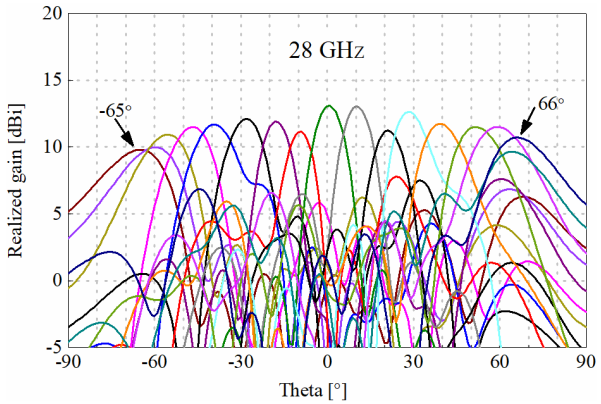

Fig. 16. Simulated beam steering of the ten-element array with reflection cancellation stubs at 28 GHz.

steerable angle range within 3 dB gain variation is 131°. Comparing with the beams at 28 GHz, the beams at 27 and 29 GHz shift to the backward and forward directions about 5°, respectively. The reason is that the proposed phased array is based on leaky-wave antenna, where the beam changes with frequency. The steerable angle range at the two frequencies is narrower than that at 28 GHz but is still larger than 110°. Thus, the proposed array can provide wide angle coverage in the 27–29 GHz band, which is sufficient to cover the 27.5–28.35 GHz band in 5G mm-wave communication.

E. Consideration of Key Parameters

There are some key parameters that have important effect on the performances of the beam-steering array.

The inter element spacing affects the sidelobe level. It is known that the inter element spacing should be less than $\lambda_0/2$ to avoid creation of grating lobes in the upper hemisphere. However, small interelement spacing will lead to strong mutual coupling among adjacent elements. In the proposed design, the optimized value is $0.44\lambda_0$.

The thickness of the upper substrate layer affects the radiation pattern of the array. The thicker is the substrate layer, the wider is the beamwidth of the patch element. A thickness value of 0.787 mm is chosen considering the available commercial substrates appropriate for Ka-band.

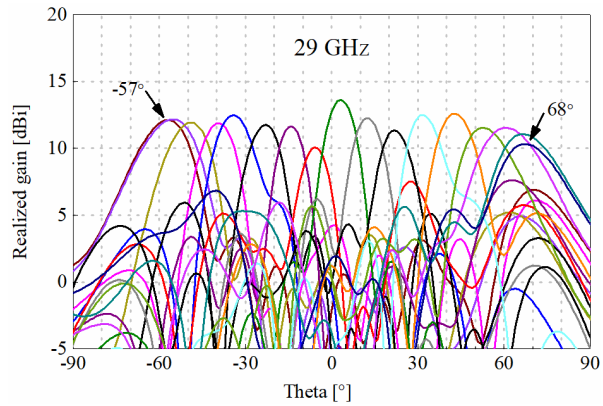

Fig. 17. Simulated beam steering of the ten-element array with reflection cancellation stubs at 29 GHz.

The thickness of the lower substrate layer affects the radiation of the feed network. This substrate thickness should be thin enough to reduce the power radiated by the microstrip line. However, the impedance of the branches for the phase shifter should be high. This leads to narrow linewidth and causes difficulty in the fabrication. A substrate thickness of 0.203 mm is adopted to make sure that the minimal linewidth is larger than 0.2 mm.

The relative dielectric constant of the lower layer affects the phase shift range of the transmission line. The physical space among elements must be less than $\lambda_0/2$. To increase the electrical length and obtain sufficient phase shift, the dielectric constant should be relatively large. A substrate with dielectric constant of 3.55 is adopted for the proposed design.

III. Analysis of Switch Impacts

In order to evaluate the effect of switch ON the performances, practical switches with bias network are studied. Fig. 18 shows the prototype of one element with practical bias circuit and p-i-n diode switches. Each element has four diodes. The two diodes at the same side of the transmission line share the same dc bias circuit. There are commercially available diodes and bias networks that can operate at 5G mm-waveband, such as MA4AGP907 p-i-n diode and MA4BN1840-1 bias network [35], [36]. In this design, conventional open-circuit microstrip lines with length of $\lambda_g/2$ are used to work as the dc-bias lines. The shunt pad for the dc wire is placed at the virtually short-circuit point, which is $\lambda_g/4$ away from the open end of the dc-bias line.

Fig. 18(b) shows the equivalent circuit of the p-i-n diode. The diode works as a resistor when the bias voltage is ON and works as a capacitor when the bias voltage is OFF. The values of the two equivalent components are the key factors that determine the insertion loss and isolation level of the diode. According to the datasheet of MA4AGP907 diode, the typical value of the resistor is 5 Ω, and the insertion loss at 28 GHz is about 0.3 dB; the typical value of the capacitor is 0.02 pf, and the isolation level at 28 GHz is about 12 dB.

The states of switches with different bias voltages are listed in Table II. Only one diode will be ON when the phase shifter works. Voltage V_1 is used to control the states of

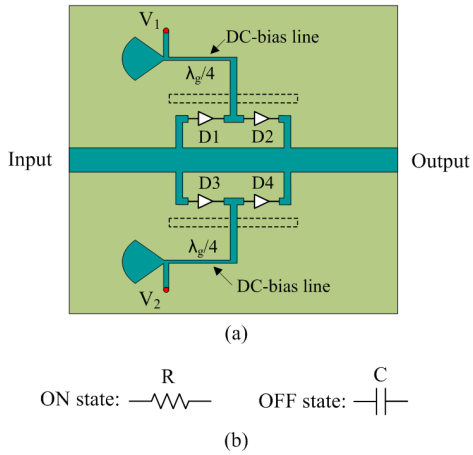

Fig. 18. Element with diodes and bias network. (a) Practical model with four diodes. (b) Equivalent circuit of the diode.

TABLE II
STATES OF P-I-N DIODES WITH DIFFERENT BIAS VOLTAGES

V_1*	V_2	D1	D2
+5V	0V	OFF	ON
0V	0V	OFF	OFF
-5V	0V	ON	OFF

* The forward biasing current is set to 10 mA.

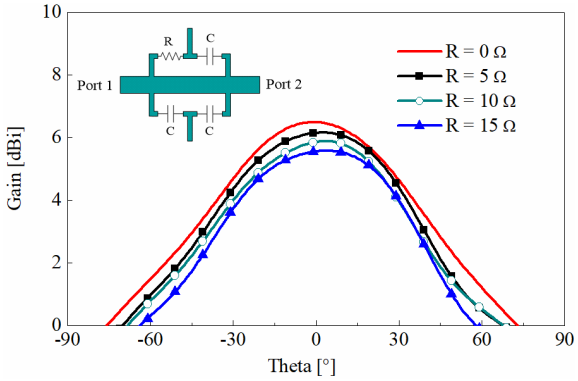

Fig. 19. Influence of equivalent resistor on the gain of element at 28 GHz.

diodes D1 and D2. Both diodes are OFF, if V_1 is 0 V. The positive or negative V_1 will turn on either D1 or D2. The forward biasing current is set to 10 mA. V_2 is always 0 V to turn off D3 and D4.

Based on the equivalent circuits, the impact of the practical switches ON the antenna performance can be evaluated. Figs. 19 and 20 show the effect of equivalent resistor and capacitor on the element that uses four switches. The dc bias voltage is controlled so that only one switch is ON and the other three are OFF. The diodes are replaced with equivalent circuits to simulate ON and OFF states. In Fig. 19, it is shown that the peak gain decreases with the increase in R. Comparing with the ideal case (R = 0 Ω), the peak gain of

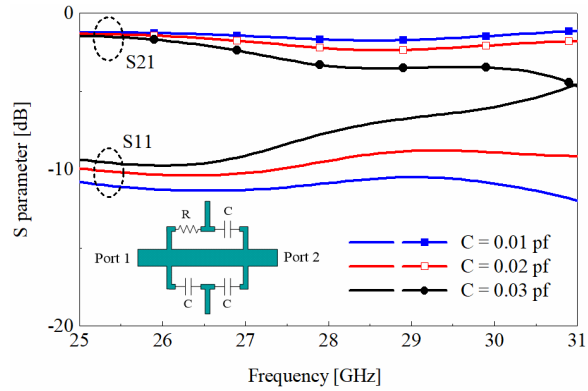

Fig. 20. Influence of equivalent capacitor on the S-parameters of element.

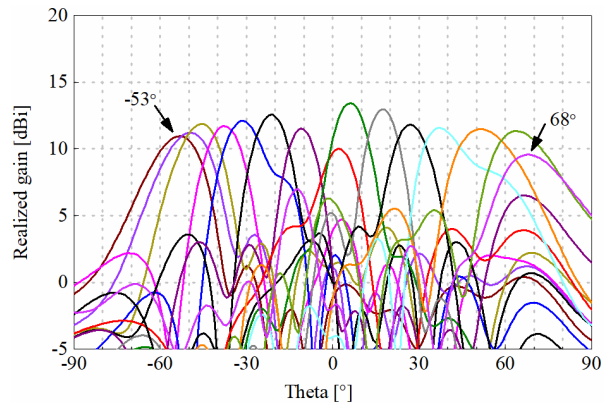

Fig. 21. Simulated beam steering of the ten-element array with practical switches at 28 GHz.

the element drops to 0.35 dB when practical switches are used (R = 5 Ω). It implies that the switches cause 0.35 dB loss on the element. In Fig. 20, it is observed that S21 becomes shallow, and S11 becomes deep, as the value of capacitor decreases. Compared with the ideal case in Fig. 4, it is known that smaller capacitor can reduce the performance difference between ideal and practical cases.

The proposed array is resimulated using the equivalent circuits of the diodes. Fig. 21 shows the beam steering at 28 GHz. The broadside beam shifts about 7° toward the forward direction. The steering angle range with 3 dB gain variation is 121°. Compared with the prototype with ideal switches, the practical switches reduce the angle range about 10°. The total radiation efficiency of all the beams varies from 54% to 75%. It implies that the overall loss of the array, including mismatch loss, residual loss, ohmic and dielectric loss, and switch loss, is less than 3 dB in the steering range.

Table III compares the proposed design with other series-fed phased arrays. It is clear that the operating frequency of the proposed array is much higher, which operates at mm-waveband. The steering angle range of the proposed array has large advantage over the referenced arrays. Therefore, the proposed array is more suitable for 5G mm-wave mobile terminal that requires wide spatial coverage.

IV. EXPERIMENTAL RESULTS

The proposed phased array is fabricated and tested. Owing to the limitation of our fabrication ability, practical switches

TABLE III
COMPARISON OF THE PROPOSED DESIGN WITH OTHER REFERENCED ANTENNAS

Ref	Frequency (GHz)	Diode type	Steering range
[27]	6	PIN	70°
[28]	6	PIN	29°
[31]	5	PIN	94°
[30]	5.5	Varactor	45°
[34]	4.5	Varactor	72°
Proposed	28	PIN	121°

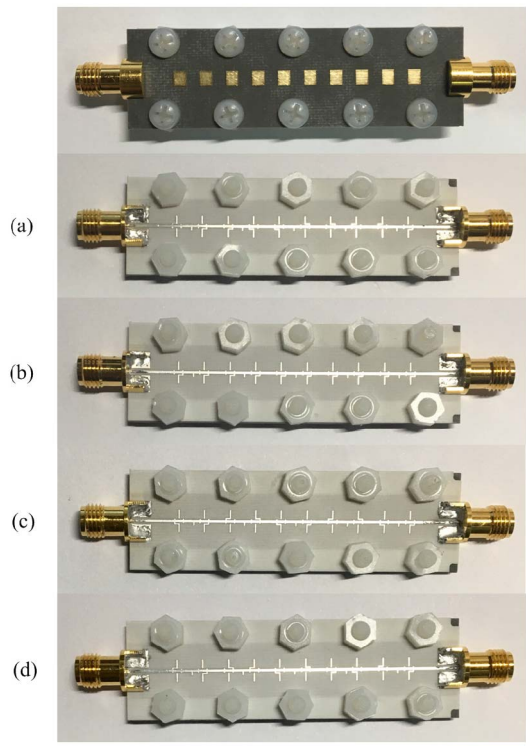

Fig. 22. Photograph of the four fabricated prototypes with different phase shifts. (a) −140°. (b) −90°. (c) 0°. (d) 140°.

are not soldered. Metal strip is used to connect the two sides of the switch in ON-state. From the analysis in Section III, it is concluded that this simplification has little influence on the feasibility verification of the prototype.

Four prototypes with different feed networks are fabricated. Fig. 22 shows the photograph of the four prototypes, which have a phase shift step of −140°, −90°, 0°, and 140°. In each prototype, the size of the two substrate layers is extended. Ten plastic screws are used to fasten the two layers tightly. Two K-type connectors are soldered on each transmission line.

Fig. 23 shows the simulated and measured S-parameters. At 28 GHz, the measured reflection coefficients are all below −7 dB, and the transmission coefficients are less than −10 dB. As mentioned in Fig. 4, the transmission coefficients can be

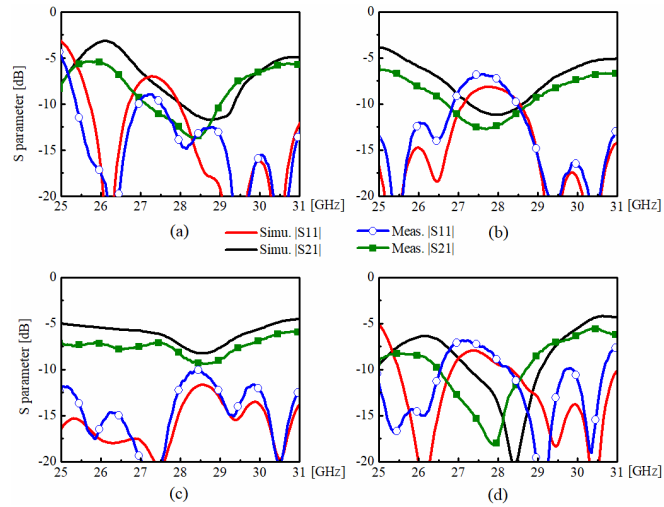

Fig. 23. Simulated and measured S-parameters of the four prototypes with phase shift of (a) −140°, (b) −90°, (c) 0°, and (d) 140°.

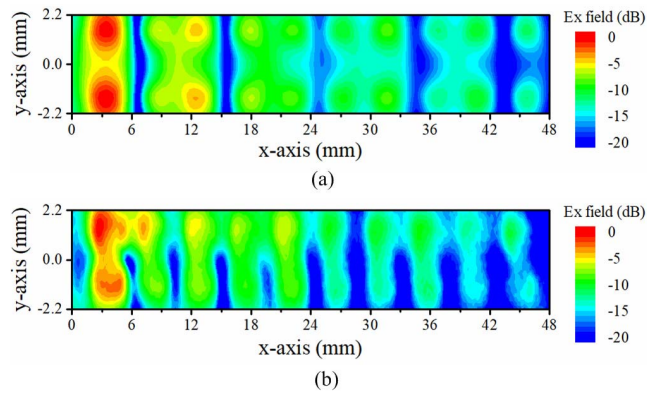

Fig. 24. Near-field distribution of the second prototype at 28 GHz. (a) Simulation. (b) Measurement with Neoscan [37].

further reduced if the leak rate of the array is increased. There is some difference between the simulated and measured results. In order to better understand the source of this difference, the near field above the array is examined. Choosing the second prototype, for example, Fig. 24 shows the simulated and measured near-field distributions, which are 1 mm above the array. The simulated data are obtained from CST tool, while the measured data are obtained by using the NeoScan platform [37]. Strong intensity is observed above the patches. The measured distribution is not symmetrical with respect to the y-axis. It implies that there can be a very small nonuniformity or gaps between the two substrates. The screws can be replaced with bonding film layer to reduce the error.

The radiation patterns are measured in a far-field chamber. The output is terminated with a 30 dB attenuator to absorb the residual energy. Fig. 25 shows the simulated and measured radiation patterns in the steering plane at 28 GHz. The simulated and measured results have reasonable agreements. It is seen that the measured peak realized gains of (a)–(d) are 8.9, 11.1, 11.7, and 9.8 dBi. The corresponding beam directions are −56°, −34°, 0°, and 58°. The cross polarizations are all below −20 dB in the main beam range. The experimental results verify the feasibility of the proposed design.

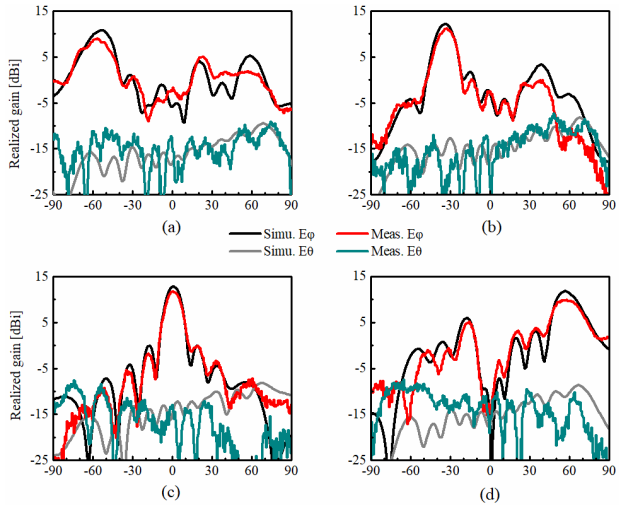

Fig. 25. Simulated and measured realized gains of the four prototypes at 28 GHz with phase shift of (a) −140°, (b) −90°, (c) 0°, and (d) 140°.

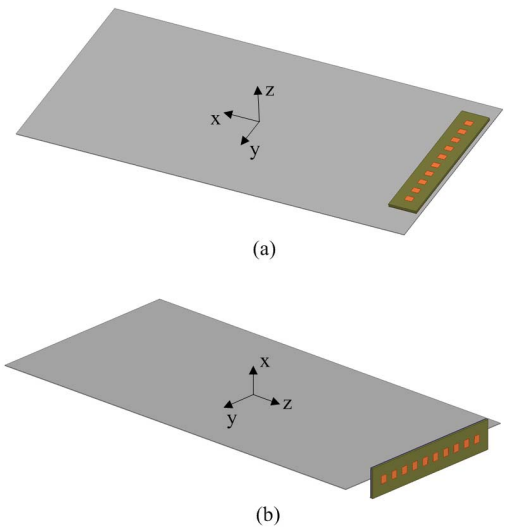

Fig. 26. Two location arrangements in the mobile terminals. (a) Horizontal arrangement. (b) Vertical arrangement.

V. Spatial Coverage in the Mobile Terminal

The spatial coverage of the proposed phased array within 5G mobile terminal is analyzed. Fig. 26 shows two typical location arrangements of the proposed array in the 5G mobile terminal. One is horizontally placed above the chassis ground and is aligned with the short edge. The other one is vertically placed with the chassis ground and can be implemented with the frame. The distance between the array and the chassis ground is 2 mm in both arrangements. The size of the chassis ground is 140 × 70 mm^2. The S-parameters of the array remain stable in the two arrangements and are not shown for brevity.

It is clear that at least two arrays are required to provide full space signal coverage, since the proposed patch array is directional. Only one array in hemisphere is discussed owing to symmetry. The spatial coverage of the two arrangements in the upper hemisphere is calculated. To avoid frequently switching among different beams, the steering angle step is set as 10°. Thus, there are 19 beams in the upper hemisphere. However, considering the maximum steerable angle range in practice, only 17 beams are adopted, which correspond to the angle ranged from −80° to +80°.

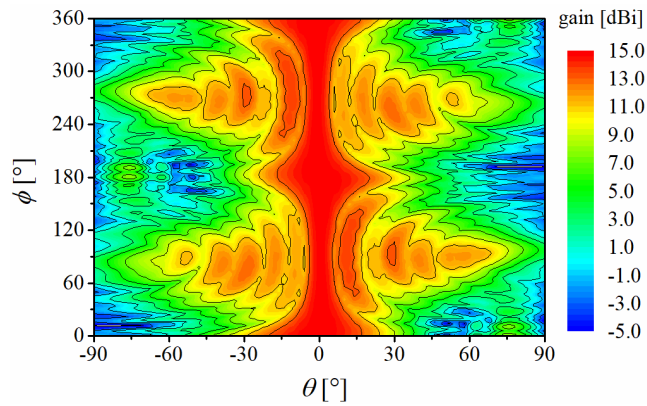

Fig. 27. Synthesized radiation pattern of horizontal arrangement at 28 GHz.

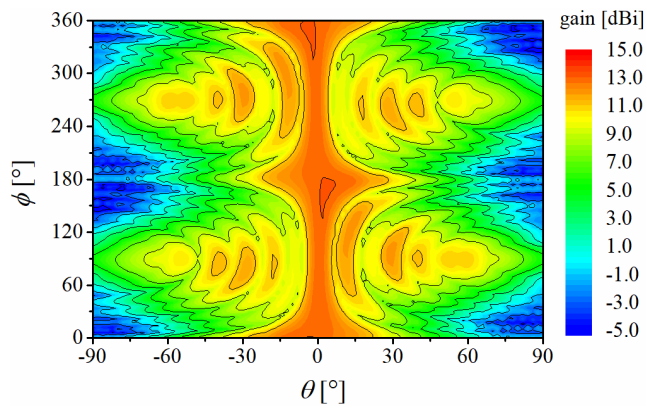

Fig. 28. Synthesized radiation pattern of vertical arrangement at 28 GHz.

By selecting the maximum of the 17 beams at each point, the optimized radiation patterns in the hemisphere can be obtained. Figs. 27 and 28 show the synthesized patterns of the two arrangements, which represent the hybrid coverage of all the beams. In Figs. 27 and 28, planes of Phi = 90° and 270° represent the scanning plane. It is observed that the intensity is strong when the angle is near the broadside direction. The signal becomes weak as the angle approaches the endfire direction. The maximum realized gain of the horizontal arrangement is larger than that of the vertical arrangement.

To quantitatively evaluate the spatial coverage of the two arrangements, the notation of solid angle coverage efficiency is defined as follows [38]:

$$Efficiency = \frac{Steerable\ solid\ angle}{Maximal\ solid\ angle}\Big|_{gain\ threshold}. \quad (5)$$

In this design, the maximum solid angle is 2π, since only half sphere is considered. The spatial coverage is calculated based on the data in Figs. 27 and 28. The corresponding spatial coverage efficiency versus different gain thresholds is shown in Fig. 29. It is observed that the two curves have similar trend. Both have excellent coverage efficiency performance. The horizontal arrangement has better coverage when the realized gain threshold is high (>8 dBi). The spatial coverage

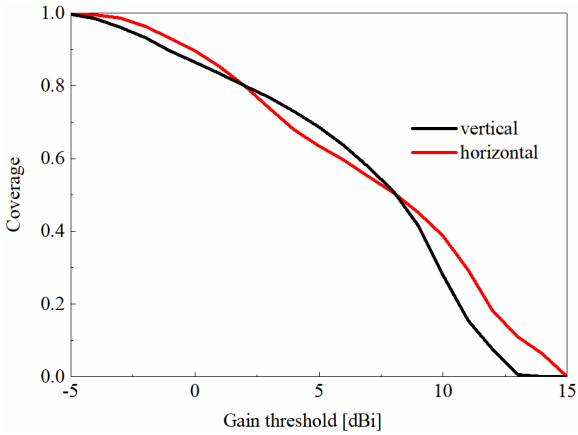

Fig. 29. Solid angle coverage efficiency for the two arrangements.

efficiency of the vertical arrangement is high when the gain threshold is medium (>3 dBi). Therefore, this evaluation provides useful information for location arrangement.

VI. Conclusion

This article presents a series-fed phased array based on patch antennas for 5G mobile terminal at mm-waveband. The required phase shifts are realized by utilization of transmission lines and switches. By introducing switches fed by tapped lines along the length of the microstrip transmission line, a series of 2 bit phase shifters are constructed with low cost and low loss. The radiating patches and the feed network are separated by the ground plane, which is helpful to broaden the steerable angle. Reflection cancellation stubs are added to overcome the gain drop at the broadside direction. Steerable angle range of 121° with 3 dB gain variation is achieved. Two typical arrangements of the array in the mobile terminal are discussed. Both have wide spatial coverage with high-gain threshold. With the advantages of having wide spatial coverage and simple phase shift mechanism, the proposed array is a promising candidate as a 5G mm-wave beam-steering antenna for mobile terminals.

Acknowledgment

The authors would like to thank Prof. Z. Jiang from Southeast University, Nanjing, China, for his help in far-field measurement. The NeoScan system used in the measurement was acquired from EMAG Technologies, Ann Arbor, MI, USA, in which Prof. Sarabandi is a Principal.

References

[1] T. S. Rappaport *et al.*, "Millimeter wave mobile communications for 5G cellular: It will work!" *IEEE Access*, vol. 1, pp. 335–349, 2013.

[2] J. G. Andrews *et al.*, "What will 5G be?" *IEEE J. Sel. Areas Commun.*, vol. 32, no. 6, pp. 1065–1082, Jun. 2014.

[3] T. S. Rappaport *et al.*, "Overview of millimeter wave communications for fifth-generation (5G) wireless networks-with a focus on propagation models," *IEEE Trans. Antennas Propag.*, vol. 65, no. 12, pp. 6213–6230, Dec. 2017.

[4] FCC. *Fact Sheet: Spectrum Frontiers Order to Identify, Open Up Vast Amounts of New High-Band Spectrum for Next Generation (5G) Wireless Broadband*. Accessed: Apr. 13, 2019. [Online]. Available: https://apps.fcc.gov/edocs_public/attachmatch/DOC-340310A1.pdf

[5] W. Hong, K.-H. Baek, and S. Ko, "Millimeter–wave 5G antennas for smartphones: Overview and experimental demonstration," *IEEE Trans. Antennas Propag.*, vol. 65, no. 12, pp. 6250–6261, Dec. 2017.

[6] Qualcomm. *Another First on Our Path to 5G NR Commercialization*. [Online]. Available: https://www.qualcomm.com/news/onq/2017/12/21/another-first-our-path-5g-nr-commercialization

[7] Huawei. *Huawei Releases First 5G Customer-Premises Equipment*. [Online]. Available: https://www.huawei.com/en/press-events/news/2018/2/5G-Customer-premises-Equipment

[8] H.-T. Kim *et al.*, "A 28-GHz CMOS direct conversion transceiver with packaged 2×4 antenna array for 5G cellular system," *IEEE J. Solid-State Circuits*, vol. 53, no. 5, pp. 1245–1259, May 2018.

[9] W. Hong, K. Baek, Y. Lee, and Y. Geon Kim, "Design and analysis of a low-profile 28 GHz beam steering antenna solution for future 5G cellular applications," in *IEEE MTT-S Int. Microw. Symp. Dig.*, Jun. 2014, pp. 1–4.

[10] N. Ojaroudiparchin, M. Shen, S. Zhang, and G. F. Pedersen, "A switchable 3-D-coverage-phased array antenna package for 5G mobile terminals," *IEEE Antennas Wireless Propag. Lett.*, vol. 15, pp. 1747–1750, 2016.

[11] J. Bang and J. Choi, "A SAR reduced mm-wave beam–steerable array antenna with dual–mode operation for fully metal–covered 5G cellular handsets," *IEEE Antennas Wireless Propag. Lett.*, vol. 17, no. 6, pp. 1118–1122, Jun. 2018.

[12] I. Syrytsin, S. Zhang, G. F. Pedersen, K. Zhao, T. Bolin, and Z. Ying, "Statistical investigation of the user effects on mobile terminal antennas for 5G applications," *IEEE Trans. Antennas Propag.*, vol. 65, no. 12, pp. 6596–6605, Dec. 2017.

[13] B. Yang, Z. Yu, Y. Dong, J. Zhou, and W. Hong, "Compact tapered slot antenna array for 5G millimeter–wave massive MIMO systems," *IEEE Trans. Antennas Propag.*, vol. 65, no. 12, pp. 6721–6727, Dec. 2017.

[14] S. X. Ta, H. Choo, and I. Park, "Broadband printed–dipole antenna and its arrays for 5G applications," *IEEE Antennas Wireless Propag. Lett.*, vol. 16, pp. 2183–2186, 2017.

[15] I. Syrytsin, S. Zhang, G. F. Pedersen, and A. S. Morris, "Compact quad–mode planar phased array with wideband for 5G mobile terminals," *IEEE Trans. Antennas Propag.*, vol. 66, no. 9, pp. 4648–4657, Sep. 2018.

[16] M. Khalily, R. Tafazolli, P. Xiao, and A. A. Kishk, "Broadband mm-wave microstrip array antenna with improved radiation characteristics for different 5G applications," *IEEE Trans. Antennas Propag.*, vol. 66, no. 9, pp. 4641–4647, Sep. 2018.

[17] M. Stanley, Y. Huang, H. Wang, H. Zhou, A. Alieldin, and S. Joseph, "A capacitive coupled patch antenna array with high gain and wide coverage for 5G smartphone applications," *IEEE Access*, vol. 6, pp. 41942–41954, 2018.

[18] W. El-Halwagy, R. Mirzavand, J. Melzer, M. Hossain, and P. Mousavi, "Investigation of wideband substrate–integrated vertically–polarized electric dipole antenna and arrays for mm-wave 5G mobile devices," *IEEE Access*, vol. 6, pp. 2145–2157, 2018.

[19] Y. Li and K.-M. Luk, "A multibeam end–fire magnetoelectric dipole antenna array for millimeter–wave applications," *IEEE Trans. Antennas Propag.*, vol. 64, no. 7, pp. 2894–2904, Jul. 2016.

[20] Q.-L. Yang, Y.-L. Ban, K. Kang, C.-Y.-D. Sim, and G. Wu, "SIW multibeam array for 5G mobile devices," *IEEE Access*, vol. 4, pp. 2788–2796, 2016.

[21] W. Hong *et al.*, "Multibeam antenna technologies for 5G wireless communications," *IEEE Trans. Antennas Propag.*, vol. 65, no. 12, pp. 6231–6249, Dec. 2017.

[22] Y. Li, J. Wang, and K.-M. Luk, "Millimeter–wave multibeam aperture–coupled magnetoelectric dipole array with planar substrate integrated beamforming network for 5G applications," *IEEE Trans. Antennas Propag.*, vol. 65, no. 12, pp. 6422–6431, Dec. 2017.

[23] B. Yu, K. Yang, C.-Y.-D. Sim, and G. Yang, "A novel 28 GHz beam steering array for 5G mobile device with metallic casing application," *IEEE Trans. Antennas Propag.*, vol. 66, no. 1, pp. 462–466, Jan. 2018.

[24] R. Movahedinia, A.-R. Sebak, M. R. Chaharmir, M. Ranjbar Nikkhah, and A. A. Kishk, "*X*-band circularly polarized electronically steerable parasitic array radiator of DRA," *IEEE Trans. Antennas Propag.*, vol. 66, no. 2, pp. 721–728, Feb. 2018.

[25] S. Zhang, I. Syrytsin, and G. F. Pedersen, "Compact beam–steerable antenna array with two passive parasitic elements for 5G mobile terminals at 28 GHz," *IEEE Trans. Antennas Propag.*, vol. 66, no. 10, pp. 5193–5203, Oct. 2018.

[26] A. B. Constantine, *Antenna Theory: Analysis and Design*. New York, NY, USA: Wiley, 2005.

[27] R. O. Ouedraogo, E. J. Rothwell, and B. J. Greetis, "A reconfigurable microstrip leaky–wave antenna with a broadly steerable beam," *IEEE Trans. Antennas Propag.*, vol. 59, no. 8, pp. 3080–3083, Aug. 2011.
[28] D. K. Karmokar, K. P. Esselle, and S. G. Hay, "Fixed–frequency beam steering of microstrip leaky–wave antennas using binary switches," *IEEE Trans. Antennas Propag.*, vol. 64, no. 6, pp. 2146–2154, Jun. 2016.
[29] M. H. Habaebi, M. Janat, and I. M. Rafiqul, "Beam steering antenna array for 5G telecommunication systems applications," *Prog. Electromagn. Res. M*, vol. 67, pp. 197–207, 2018.
[30] M. Wang, H. F. Ma, H. C. Zhang, W. X. Tang, X. R. Zhang, and T. J. Cui, "Frequency–fixed beam–scanning leaky–wave antenna using electronically controllable corrugated microstrip line," *IEEE Trans. Antennas Propag.*, vol. 66, no. 9, pp. 4449–4457, Sep. 2018.
[31] L. Chang, Y. Li, Z. Zhang, and Z. Feng, "Reconfigurable 2-bit fixed–frequency beam steering array based on microstrip line," *IEEE Trans. Antennas Propag.*, vol. 66, no. 2, pp. 683–691, Feb. 2018.
[32] T. Lou, X.-X. Yang, H. Qiu, Q. Luo, and S. Gao, "Low–cost electrical beam–scanning leaky–wave antenna based on bent corrugated substrate integrated waveguide," *IEEE Antennas Wireless Propag. Lett.*, vol. 18, no. 2, pp. 353–357, Feb. 2019.
[33] Y. Geng *et al.*, "Radiation pattern-reconfigurable leaky-wave antenna for fixed-frequency beam steering based on substrate-integrated waveguide," *IEEE Antennas Wireless Propag. Lett.*, vol. 18, no. 2, pp. 387–391, Feb. 2019.
[34] K. Chen *et al.*, "An electronically controlled leaky-wave antenna based on corrugated SIW structure with fixed-frequency beam scanning," *IEEE Antennas Wireless Propag. Lett.*, vol. 18, no. 3, pp. 551–555, Mar. 2019.
[35] *MA4AGP907*. Accessed: Aug. 22, 2019. [Online]. Available: https://www.macom.com/products/product-detail/MA4AGP907
[36] *MA4BN1840-1*. Accessed: Aug. 22, 2019. [Online]. Available: https://www.macom.com/products/product-detail/MA4BN1840-1
[37] *NEOSCAN: Ultra-Wideband Non-Invasive Field Measurement System*. Accessed: Feb. 20, 2019. [Online]. Available: https://emagtech.com/neoscan-system/
[38] J. Helander, K. Zhao, Z. Ying, and D. Sjoberg, "Performance analysis of millimeter-wave phased array antennas in cellular handsets," *IEEE Antennas Wireless Propag. Lett.*, vol. 15, pp. 504–507, 2016.

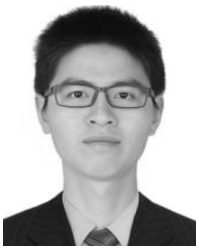

Changjiang Deng (Member, IEEE) was born in Loudi, Hunan, China. He received the B.S. degree in communication engineering from the Beijing University of Posts and Telecommunications (BUPT), Beijing, China, in 2011 and the Ph.D. degree in electrical engineering from Tsinghua University, Beijing, in 2016.

He is currently an Assistant Professor with the School of Information and Electronics, Beijing Institute of Technology, Beijing. His research interests include mobile phone antennas, dual-polarized antennas, circularly polarized antennas, and MIMO antennas.

Di Liu was born in Hengshui, Hebei, China, in 1994. She received the B.S. degree in electronic information engineering from Tongji University, Shanghai, China, in 2017. She is currently pursuing the M.S. degree with the Beijing Institute of Technology, Beijing, China.

Her current research interests include small antennas for handset device and MIMO antennas.

Behzad Yektakhah (Student Member, IEEE) received the B.S. and M.S. degrees in electrical engineering from the University of Tehran, Tehran, Iran, in 2008 and 2011, respectively, and the Ph.D. degree in electrical engineering from the University of Michigan, Ann Arbor, MI, USA, in 2018.

His research focuses on radar through-the-wall and subsurface imaging, electromagnetic scattering, and antennas.

Kamal Sarabandi (Fellow, IEEE) received the B.S. degree in electrical engineering from the Sharif University of Technology, Tehran, Iran, in 1980, and the M.S. degree in electrical engineering, the M.S. degree in mathematics, and the Ph.D. degree in electrical engineering from the University of Michigan, Ann Arbor, MI, USA, in 1986 and 1989, respectively.

He is currently the Director of the Radiation Laboratory and the Rufus S. Teesdale Endowed Professor of engineering with the Department of Electrical Engineering and Computer Science, University of Michigan. He led the Center for Microelectronics and Sensors, University of Michigan, sponsored by the Army Research Laboratory under the Micro-Autonomous Systems and Technology (MAST) Collaborative Technology Alliance (CTA) Program from 2008 to 2018. He is currently leading a newly established center in microwave sensor technology. He has authored many book chapters and more than 280 articles in refereed journals on miniaturized and on-chip antennas, meta-materials, electromagnetic scattering, wireless channel modeling, random media modeling, microwave measurement techniques, radar calibration, inverse scattering problems, and microwave sensors. He has also authored more than 650 articles and invited presentations in many national and international conferences and symposia on similar subjects. His research areas of interests include microwave and millimeter-wave radar remote sensing, meta-materials, electromagnetic wave propagation, and antenna miniaturization.

Dr. Sarabandi served as a member of the NASA Advisory Council appointed by the NASA Administrator for two consecutive terms from 2006 to 2010. He was a member of the Editorial Board of the PROCEEDINGS OF THE IEEE and an Associate Editor of the IEEE TRANSACTIONS ON ANTENNAS AND PROPAGATION and the IEEE SENSORS JOURNAL. He is a member of the Commissions F and B of URSI and is serving as the Chair of the USNC URSI Commission F. He received the Henry Russel Award from the Regent of the University of Michigan in 1997, the GAAC Distinguished Lecturer Award from the German Federal Ministry for Education, Science, and Technology, in 1999, the 1996 EECS Department Teaching Excellence Award, the IEEE Geoscience and Remote Sensing Society (GRSS) Distinguished Achievement Award and the University of Michigan Faculty Recognition Award in 2005, the Best Paper Award at the 2006 Army Science Conference, the IEEE GRSS Symposium Best Paper Award in 2008 and 2017, the Humboldt Research Award from The Alexander von Humboldt Foundation of Germany in 2008, the 2010 Distinguished Faculty Achievement Award from the University of Michigan, and the 2011 IEEE Judith A. Resnik Award from the IEEE Board of Directors. He was recognized by IEEE GRSS with its 2013 Education Award. He received the College of Engineering Research Excellence Award in 2004, the Stephen S. Attwood Award in 2017, and the Ted Kennedy Family Faculty Team Excellence Award from the College of Engineering at the University of Michigan in 2018. He was recognized as one of the top 50 graduates of the Sharif University of Technology in 2016. He also received the NASA Group Achievement Award for his contributions to the NASA SMAP Mission. In the past several years, joint articles presented by his students at a number of international symposia (IEEEAPS'95,'97,'00,'01,'03,'05,'06,'07, and'16; IEEE IGARSS'99,'02,'07,'11, and'14; IEEE IMS'01; USNC URSI'04,'05,'06,'10, and '11; AMTA'06; URSI GA '08 and'14; and Eastern Snow Conference'16) have received the best paper awards. He served as the President of IEEE GRSS in 2015 and 2016.